Droplet dynamics driven by electrowetting

Ke Xiao*
Department of Physics and Fujian Provincial Key Laboratory for Soft Functional Materials Research, College of Physical Science and Technology, Xiamen University, Xiamen 361005, People's Republic of China and Wenzhou Institute, University of Chinese Academy of Sciences, Wenzhou 325016, People's Republic of China

Chen-Xu Wu†
Department of Physics and Fujian Provincial Key Laboratory for Soft Functional Materials Research, College of Physical Science and Technology, Xiamen University, Xiamen 361005, People's Republic of China

(Received 26 March 2022; accepted 31 May 2022; published 27 June 2022)

Even though electrowetting-on-dielectric (EWOD) is a useful strategy in a wide array of biological and engineering processes with numerous droplet-manipulation applications, there is still a lack of complete theoretical interpretation on the dynamics of electrowetting. In this paper we present an effective theoretical model and use the Onsager variational principle to successfully derive general dynamic shape equations for electrowetting droplets in both the overdamped and underdamped regimes. It is found that the spreading and retraction dynamics of a droplet on EWOD substrates can be fairly well captured by our model, which agrees with previous experimental results very well in the overdamped regime. We also confirm that the transient dynamics of EW can be characterized by a timescale independent of liquid viscosity, droplet size, and applied voltage. Our model provides a complete fundamental explanation of EW-driven spreading dynamics, which is important for a wide range of applications, from self-cleaning to novel optical and digital microfluidic devices.

DOI: 10.1103/PhysRevE.105.064609

I. INTRODUCTION

Electrowetting-on-dielectric (EWOD), a phenomenon referring to the effect of electric fields on the wetting of a droplet on a dielectric-layer-covered electrode surface, is an important and versatile technique via droplet manipulation [1]. So far it has attracted considerable attention due to its significance in fundamental scientific understanding and numerous technological applications, such as novel digital microfluidic devices [2–5], fast response displays [6], fast optical imaging [7], optical devices [8,9], inkjet/soft printing [10,11], self-cleaning [12], anti-icing [13,14], and inducing droplet detachment [15] and wetting transition [16]. To improve the performance of such applications, a fundamental understanding of droplet dynamics driven by electrowetting (EW) is crucial [17]. It has been found that this spreading motion of a droplet on a solid substrate is initiated by the electrical force concentrated near the three-phase contact line (TCL), of which the dynamics is determined by the balance among the driving electrical force, capillary force, and resistance forces (i.e., contact line friction). Earlier studies have revealed that the EW-driven spreading dynamics can be typically categorized into two main regimes, namely, the overdamped and the underdamped regimes [18,19]. In the overdamped regime, dynamic behaviors are dominated by viscous effects [18–22], whereas in the underdamped regime, the droplet inertia becomes dominant [18,19,23,24].

During the past decade, numerous efforts of experiments [18,19,24–26], theoretical modelings [27,28], and numerical simulations [29,30] have been devoted to getting a better understanding of the spreading dynamics triggered by the EW effect. For example, the dynamic EW and dewetting of ionic liquids have been investigated with high-speed video microscopy, and the experimental measurements have shown that the base area of the droplet varies exponentially during both the EW and retraction processes. The linear dependence of dynamic contact angle on the speed of contact line expansion was examined using the hydrodynamic and molecular-kinetic models [26]. Using the domain perturbation method, Oh *et al.* [28] analyzed the unsteady motion and the shape evolution of a sessile drop actuated by EW and reached a qualitative agreement between their analytical results and experimental ones, validating their theoretical model. By studying the dependence of spreading dynamics on drop size and viscosity under various voltages, it has been found that there exists a critical viscosity at which the spreading pattern changes from an underdamped one to an overdamped one. More recently, Vo *et al.* systematically investigated the dynamics of EW droplets, derived the critical viscosity at which the transition occurs, and revealed its subtle and often hidden dependence on the EW dynamics [18]. They also reported that a transient timescale can be used to characterize both the spreading and retracting dynamics [19]. In addition, the volume-of-fluid method [29] and finite element method [30], in which the fluid dynamics is modeled by the Navier-Stokes

*xiaoke@ucas.ac.cn
†cxwu@xmu.edu.cn

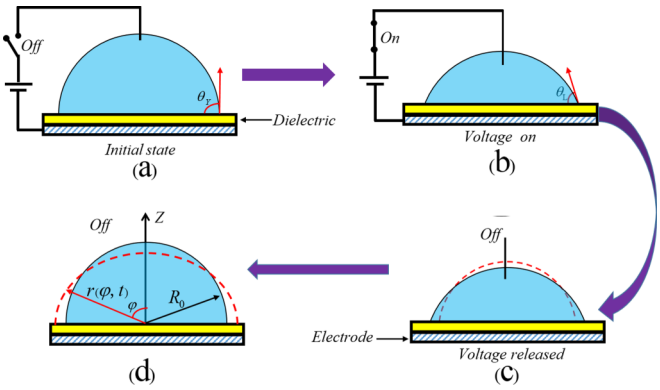

FIG. 1. Schematic pictures of a droplet on a substrate in equilibrium state with contact angle (a) θ_Y in the absence of electric voltage and (b) θ_L in the presence of electric voltage. (c) Recoiling stage and (d) the equilibrium state of the droplet in the absence of electric voltage.

equations, were also employed to study the static and the dynamic EW problems.

Despite the fact that the dynamics of droplets induced by EW has been extensively studied via either experimental or theoretical approaches, it is still hard to find a model which can be used to construct the free energy explicitly for a droplet in terms of droplet shape, especially in the underdamped regime, so that a systematic analytical understanding of the underlying subtle mechanism, in particular, the governing kinetic equations of the nonequilibrium EW dynamics and the dependence of transient dynamics in EW on liquid viscosity, droplet size, and applied voltage, can be obtained.

In this paper we establish a theoretical model to explicitly formulate the free energy of a droplet in terms of droplet shape parameters, which enables us to study the EW-driven dynamics of the droplet analytically on a dielectric-layer-covered electrode substrate. The numerical results predicted by the present model are compared with experimental ones. To explore the transient dynamics in both the overdamped and underdamped regime, we further investigate how the viscosity and the size of a droplet, and applied voltage effect the EW dynamics. We expect this work can offer some helpful implications for the design of EWOD-based devices when the physical properties of droplet (e.g., viscosity and droplet size) and applied voltage are varied to meet their requirements.

II. THEORETICAL MODELING

We begin our investigation by considering an aqueous droplet placed on a substrate consisting of an insulating surface layer (thickness d) on top (yellow) and an electrode underneath, as shown in Fig. 1. Both the droplet and the electrode are immersed in an oil fluid (e.g., the surrounding environment is a pool of silicone oil) with viscosity μ_0. The apparent contact angle θ_Y [see Fig. 1(a)] at the equilibrium state satisfies Young's equation, $\gamma_{sm} - \gamma_{ls} = \gamma_{lm}\cos\theta_Y$, where γ_{sm}, γ_{ls}, and γ_{lm} are interfacial tensions of the solid-medium, liquid-solid, and liquid-medium interfaces, respectively. When an external voltage U is applied between the droplet and the flat substrate, the accumulation of free charges near the electrode causes a reduction of the local liquid-solid surface tension γ_{ls} and subsequently induces the spreading of the droplet, yielding another equilibrium state with an apparent contact angle θ_L [see Fig. 1(b)], described by the well-known Young-Lippmann equation [1,31] $\cos\theta_L = \cos\theta_Y + \eta$, with $\eta = \varepsilon_0\varepsilon U^2/(2d\gamma_{lm})$, where η, ε_0, and ε are the dimensionless EW number, the dielectric permittivity in vacuum, and the relative dielectric constant, respectively. Here the reduced liquid-solid surface tension can be replaced by an effective one $\gamma_{ls}^{eff} = \gamma_{ls} - \eta\gamma_{lm}$. Once the electric voltage is switched off, the droplet will keep its current shape as shown in Fig. 1(c) as its transient state. However, due to a sudden increase in the local liquid-solid surface tension owing to the short discharge timescale of the droplet-electrode capacitor being much faster than the relaxation time of the droplet [32,33], the restoration of liquid-solid interfacial tension leads to a recovery effect. Subsequently, the droplet will undergo a recoiling stage and reach the final equilibrium configuration [see Fig. 1(d)], during which a flow will be induced, causing a viscous dissipation typically comprising contributions in the bulk droplet, near the substrate, and at the vicinity of the contact line [18,19,34]. In the next two sections, a theoretic model based on the Onsager variational principle is established to derive the shape (mode) equations that govern the nonequilibrium EW dynamics in the overdamped and the underdamped regimes, respectively. Here it should be noted that the effects of evaporation and gravity are neglected, and the volume of the droplet is assumed to be constant in this paper. Such an assumption is reasonable if the droplet size is smaller than the capillary length $l_c = \sqrt{\gamma_{lm}/(\rho g)}$, where ρ and g denote the droplet density and the gravitational acceleration, respectively.

A. Overdamped regime

In the presence of an electric field, the free energy is written as a sum of interfacial energies,

$$F = \gamma_{lm}A_{lm} + \gamma_{ls}^{eff}A_{ls} + \gamma_{sm}A_{sm}, \tag{1}$$

where A_{lm}, A_{ls}, and A_{sm} are the areas of the liquid-medium, solid-medium, and liquid-solid interfaces, respectively. Let $A_t = A_{sm} + A_{ls}$, and with a consideration of the Young-Lippmann equation, Eq. (1), can be converted to [16]

$$F = \gamma_{lm}A_{lm} - \gamma_{lm}A_{ls}\cos\theta_L + \gamma_{sm}A_t. \tag{2}$$

Similarly, the general form of the free energy in the absence of an electric field reads

$$F = \gamma_{lm}A_{lm} - \gamma_{lm}A_{ls}\cos\theta_Y + \gamma_{sm}A_t. \tag{3}$$

In the overdamped regime, the shape of the droplet is treated as a sphere due to the dynamic behaviors dominated by the viscous effect and the inertial effect is neglected. Thereby, for the spreading stage, the free energy of the system can be calculated as

$$F_s^o = \gamma_{lm}\pi R_b^2\left[\frac{2}{1+\cos\theta} - \cos\theta_L\right], \tag{4}$$

where R_b, θ, and θ_L represent the base radius, the dynamic contact angle, and the contact angle at equilibrium,

respectively. A time derivative of such a free energy leads to

$$\dot{F}_s^o = \gamma_{lm} 2\pi R_b \left[\dot{R}_b(t) \left(\frac{2}{1+\cos\theta} - \cos\theta_L \right) + \frac{R_b \sin\theta}{(1+\cos\theta)^2} \dot{\theta}(t) \right], \quad (5)$$

where the dots denote a derivative with respect to time t. According to conservation of volume $dV^o(t)/dt = 0$, we can obtain (see the Appendix for the detailed derivations)

$$\dot{\theta}(t) = -\frac{(2+\cos\theta)\sin\theta}{R_b} \dot{R}_b(t). \quad (6)$$

Given the equation for $\dot{\theta}(t)$, one needs one more equation for $\dot{R}_b(t)$ to describe the EW-driven droplet spreading dynamics in the overdamped regime. To get this we use the Onsager principle [35–37] to determine the evolution of the system by a minimization of the Rayleighian:

$$\Re = \dot{F} + \Phi, \quad (7)$$

where $\dot{F}$ is the time derivative of the free energy of the system given by Eq. (5), and Φ is the energy dissipation function. Typically there exist two types of descriptions accounting for droplet spreading, namely, the hydrodynamic approach [38,39] and the molecular-kinetic theory [20], depending on the dominant dissipation channel. The hydrodynamic approach ascribes the dissipation to the viscous flows generated in the bulk [38,39]. In contrast, the molecular-kinetic theory concentrates on the dissipative processes occurring in the vicinity of the contact line [20]. Strictly speaking, the total viscous dissipation is the sum of bulk dissipation and contact line dissipation. However, Brochard-Wyart and de Gennes [40] have pointed out that for large contact angles the dynamics is most likely to be dominated by the dissipation at the contact line, whereas for small contact angles, viscous dissipation in the bulk would be the governing channel. In a recent study Xu *et al.* [41] investigated the evolution of liquid film and liquid droplet moving on a solid substrate by using Onsager's variational principle, where viscous dissipation in the bulk was calculated with the contact line friction contribution excluded, as the contact angle is small. In this paper, as the contribution at the vicinity of the contact line dominates the whole dissipation process [34] in the droplet with a relatively large contact angle value, we merely consider the contribution made by the contact line, with its dissipation rate expressed as

$$\Phi_{vis}^{ct,o} = \pi \lambda R_b \dot{R}_b^2, \quad (8)$$

where λ is the friction coefficient at the contact line. Here the friction coefficient, according to Refs. [18,19,34], can be given by $\lambda = C(\mu\mu_0)^{1/2}$, where μ is the droplet viscosity, μ_0 is the viscosity of the surrounding medium of the droplet, and C is a constant depending on roughness and chemical properties of the surface [42]. Substituting Eqs. (5) and (8) into Eq. (7) and combining Eq. (6) leads to

$$\Re_o = 2\pi \gamma_{lm} R_b \dot{R}_b (\cos\theta - \cos\theta_L) + \pi \lambda R_b \dot{R}_b^2. \quad (9)$$

The Onsager principle tells us that $\dot{R}_b(t)$ is determined by the condition $\partial\Re_o/\partial\dot{R}_b$=0, which gives the evolution equation

$$\dot{R}_b = \frac{\gamma_{lm}}{\lambda}(\cos\theta_L - \cos\theta). \quad (10)$$

Similarly, in the absence of an electric field, the kinetic equation for the retracting stage can also be expressed as

$$\dot{R}_b = \frac{\gamma_{lm}}{\lambda}(\cos\theta_Y - \cos\theta). \quad (11)$$

Here the retracting motion is purely driven by capillarity.

It is well known that the driving force f per unit length pulling the liquid at the three-phase contact line is given by $f = \gamma_{lm}(\cos\theta_L - \cos\theta)$ [1,43]. Such a driving force, if combined with Eqs. (10) and (11), gives a linear relation between f and $\dot{R}_b$, indicating a balance between driving force and friction force [15,18,19,44]. The kinetic equations also reveal the dependence of dynamic contact angle on the contact line velocity. The linear dependence of $\cos\theta$ on the speed of the contact line $\dot{R}_b$ in both EW and retraction processes are consistent with the previous reports as well [26]. The quantitatively good agreement between theoretical and experimental results verifies that the droplet spreading and the droplet retraction dynamic behaviors in the overdamped regime (i.e., droplet with high viscosity) driven by EW can be described very well by Eqs. (6), (10), and (11).

Several approaches have been devoted to study the relationship between the dynamic contact angle and the contact line velocity, such as the hydrodynamic approach [38,39] and the molecular-kinetic theory [20]. Both theories predict evolution of the dynamic contact angles as a function of the contact line velocity. When dealing with the case that dynamic contact angles are small and close to the equilibrium contact angle, the relationship between the dynamic contact angle and the contact line velocity can be linearized to a form similar to Eq. (11). In fact, Eqs. (10) and (11) derived based on the Onsager's variational principle are similar to the boundary condition derived by using molecular dynamics and continuum mechanics [45]. Since the kinetic equations derived by Onsager's variational principle in the overdamped regime are direct and concise, our theoretical model shows some advantages as compared with the approaches mentioned above.

B. Underdamped regime

Experimentally, it has been reported that low droplet viscosity will lead to underdamped dynamic features during the droplet spreading process [18,24]. As a consequence, the droplet shape in this regime, though still axis symmetric, is no longer spherical. To describe the shape profile, we decompose it into Legendre polynomials with coefficients c_{2n}, i.e.,

$$r(\varphi, t) = R_0 + \sum_{n=1}^{\infty} c_{2n}(t) P_{2n}(\cos\varphi), \quad (12)$$

where R_0, $c_{2n}(t)$, P_{2n}, and φ are the effective radius of the droplet, the time-dependent amplitude of a shape mode, Legendre polynomials, and the polar angle, respectively, as shown in Fig. 1(d). It is worth noting that a 90° average contact angle is assumed.

In the situation of low-viscosity flow, the velocity flow is irrotational with a velocity $\boldsymbol{v} = \nabla\psi$, where the flow potential ψ satisfies $\Delta\psi = 0$. Here we assume the shape of the droplet is symmetric around the azimuthal angle, so that the

general solution of the Laplace equation in spherical coordinates reads $\psi(r,\varphi,t)=\sum_{l=0}^{\infty}[a_l(t)/r^{l+1}]P_l(\cos\varphi)$, where $a_l(t)$ are time-dependent coefficients. The boundary condition requires that the perpendicular velocity of the droplet must vanish on the solid substrate ($\varphi=\pi/2$), i.e., $v_\varphi=-\partial\psi/r\partial\varphi=0$. To satisfy this condition we should have $l=2n$, and the general solution can be rewritten as $\psi(r,\varphi,t)=\sum_{l=0}^{\infty}[c_{2n}(t)/r^{2n+1}]P_{2n}(\cos\varphi)$. At the surface of the droplet ($r=R_0$), the radial velocity of the droplet satisfies the boundary conditions $v_r=\partial\psi/\partial r=\dot r(\varphi,t)$. Then the flow potential can be expressed as

$$\psi=(r,\varphi,t)=-\sum_{n=0}^{\infty}\frac{R_0^{2n+2}}{(2n+1)r^{2n+1}}\dot c_{2n}(t)P_{2n}(\cos\varphi), \quad (13)$$

where $n=0$ corresponds to the contribution made by spherical symmetry and is treated separately in this paper. Similar to the previous section, the free energy can be calculated as (see the Appendix for the detailed derivations)

$$\begin{aligned}F_{\rm s}^{\rm u}=&\gamma_{\rm lm}\left[2\pi R_0^2+4\pi R_0c_0(t)+2\pi\sum_{n=1}^{\infty}\frac{n(2n+1)+1}{4n+1}c_{2n}^2(t)\right]\\&-\gamma_{\rm lm}\left[\pi R_0^2+2\pi R_0\sum_{n=1}^{\infty}c_{2n}(t)P_{2n}(0)\right]\cos\theta_{\rm L}. \quad (14)\end{aligned}$$

Constructing the free energy explicitly [Eq. (14)] in terms of droplet shape $c_{2n}(t)$ in the underdamped regime is significant, because this allows one to discuss the droplet dynamics systematically. On the other hand, the kinetic energy due to the flow of the fluid is given by [46]

$$T=\pi\rho R_0^3\sum_{n=1}^{\infty}\frac{\dot c_{2n}^2(t)}{(2n+1)(4n+1)}. \quad (15)$$

Given these, the free energy change rate $\dot E=\dot F_{\rm s}^{\rm u}+\dot T$ then is written as

$$\begin{aligned}\dot E=&4\pi\gamma_{\rm lm}R_0\dot c_0(t)+4\pi\gamma_{\rm lm}\sum_{n=1}^{\infty}\frac{n(2n+1)+1}{4n+1}c_{2n}(t)\dot c_{2n}(t)\\&-2\pi R_0\gamma_{\rm lm}\cos\theta_{\rm L}\sum_{n=1}^{\infty}\dot c_{2n}(t)P_{2n}(0)\\&+2\pi\rho R_0^3\sum_{n=1}^{\infty}\frac{\dot c_{2n}(t)\ddot c_{2n}(t)}{(2n+1)(4n+1)}, \quad (16)\end{aligned}$$

where only the first order of $P_{2n}(0)$ is considered and the dots denote a derivative with respect to time t. Under the volume conservation of the droplet $dV^{\rm u}/dt=0$, we get (see the Appendix for the detailed derivations)

$$\dot c_0(t)=-\frac{2}{R_0}\sum_{n=1}^{\infty}\frac{c_{2n}(t)\dot c_{2n}(t)}{4n+1}. \quad (17)$$

Substituting $\dot c_0(t)$ into Eq. (16), one obtains

$$\begin{aligned}\dot E=&4\pi\gamma_{\rm lm}\sum_{n=1}^{\infty}\frac{(2n-1)(n+1)}{4n+1}c_{2n}(t)\dot c_{2n}(t)\\&-2\pi R_0\gamma_{\rm lm}\cos\theta_{\rm L}\sum_{n=1}^{\infty}\dot c_{2n}(t)P_{2n}(0)\\&+2\pi\rho R_0^3\sum_{n=1}^{\infty}\frac{\dot c_{2n}(t)\ddot c_{2n}(t)}{(2n+1)(4n+1)}. \quad (18)\end{aligned}$$

The energy dissipation function in the bulk is written as [46]

$$\begin{aligned}\Phi_{\rm vis}^{\rm b,u}=&\frac{\mu}{2}\iint(\nabla v^2)\cdot{\bf n}dS\\=&2\pi\mu R_0\sum_{n=1}^{\infty}\frac{2n+2}{4n+1}\dot c_{2n}^2(t). \quad (19)\end{aligned}$$

The dissipation at the contact line is given by

$$\begin{aligned}\Phi_{\rm vis}^{\rm ct,u}=&\pi\lambda r(\varphi=\pi/2,t)\dot r^2(\varphi=\pi/2,t)\\=&\pi\lambda R_0\sum_{n=1}^{\infty}\dot c_{2n}^2(t)P_{2n}^2(0). \quad (20)\end{aligned}$$

Here we only keep to the lowest order of $P_{2n}(0)$. Therefore the governing equation for the droplet shape modes is determined by the condition $\partial\Re_{\rm u}/\partial\dot c_{2n}(t)=0$, where $\Re_{\rm u}=\dot E+\Phi_{\rm vis}^{\rm b}+\Phi_{\rm vis}^{\rm ct}$ is the Rayleighian. Substituting Eqs. (18)–(20) into $\partial\Re/\partial\dot c_{2n}(t)=0$ yields the evolution equation of shape modes,

$$\begin{aligned}&\ddot c_{2n}(t)+\left[2\mu(2n+2)+\lambda P_{2n}^2(0)(4n+1)\right]\frac{2n+1}{\rho R_0^2}\dot c_{2n}(t)\\&+\frac{\gamma_{\rm lm}}{\rho R_0^3}(2n-1)(2n+1)(2n+2)c_{2n}(t)\\&=\frac{\gamma_{\rm lm}}{\rho R_0^2}(2n+1)(4n+1)P_{2n}(0)\cos\theta_{\rm L}. \quad (21)\end{aligned}$$

The solution to Eq. (21) gives the transient shape mode of EW droplets (see also Refs. [28] and [47]).

III. RESULTS AND DISCUSSION

Our calculation is carried out by using the values of parameters $\varepsilon=1.93$, $d=2.5$ mm, $\mu_0=4.6$ mPa s, and $C=26.24$ [19]. The controlling parameters U, μ, $\gamma_{\rm lm}$, and V_0 are given in the corresponding figures.

A. Overdamped regime

In the overdamped regime, in order to numerically solve Eqs. (6), (10), and (11), and compare our theoretical results with the experimental ones, we use the same values of parameters as those in Refs. [18] and [19], i.e., $\gamma_{\rm lm}=26.9$ mN m^{-1} and $\theta_{\rm Y}=165.4^\circ$. In Fig. 2(a), theoretical curves (black and blue lines) of base radius $R_{\rm b}$ and contact angle θ based on the present model are displayed to compare with the experimental results (olive circle and red diamond dots) in Ref. [19]. It is shown in the figure that our theoretical prediction agrees considerably well, both in the spreading and the retraction stages, with the experimental results reported by Vo *et al.* [19], indicating that our theoretical model is a convincing one. To further capture the dynamic features of the EW and the retraction process, we plot the TCL velocity $u=\dot R_{\rm b}$ against time t for these two stages, as illustrated in Fig. 2(b). It is

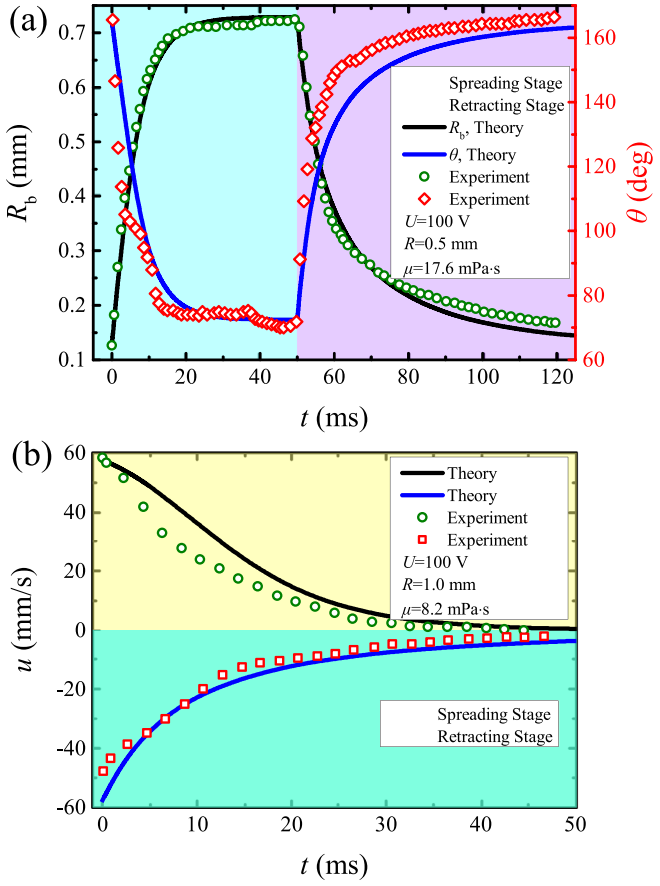

FIG. 2. Comparison of theoretical time-dependent (a) base radius R_b and contact angle θ, and (b) contact line velocity u with those measured in Ref. [19]. $\theta_Y = 165.4^\circ$ is used for calculation.

found that the contact line velocity monotonically reduces to zero, a conclusion again in very good agreement with that obtained by Vo *et al.* [19] (circle and square symbol), where the black line and circle symbol refer to the spreading stage, and the blue line and square symbol correspond to the retraction process, respectively. The monotonic variation trend of R_b, θ, and u demonstrates that the contact line, in both spreading and retraction stages, evolves in an overdamped way. The reason lies in that the liquid inertia effect can be neglected and viscosity becomes a dominant factor causing the droplet to spread or retract gradually to its equilibrium state. In particular, contact line friction dissipates most excessive interfacial energy in the overdamped regime.

Here it should be noted that in the overdamped regime, the viscous dissipation in the bulk is assumed to be negligible due to the small velocity gradient. In fact, there exist characteristic timescales τ_o for the transient dynamics of viscous droplets actuated by EW. The balance between the maximum driving force and the contact line friction force yields a characteristic timescale $\tau_o = \lambda(R_e - R_0)/(\eta\gamma_{lm})$ [19], which represents the timescale for a droplet to switch between the initial and the final equilibrium states. To confirm that τ_o is the characteristic timescale for the transient dynamics of droplet spreading and retraction in an ambient environment, we first respectively exhibit the temporal evolution of the base radius for various

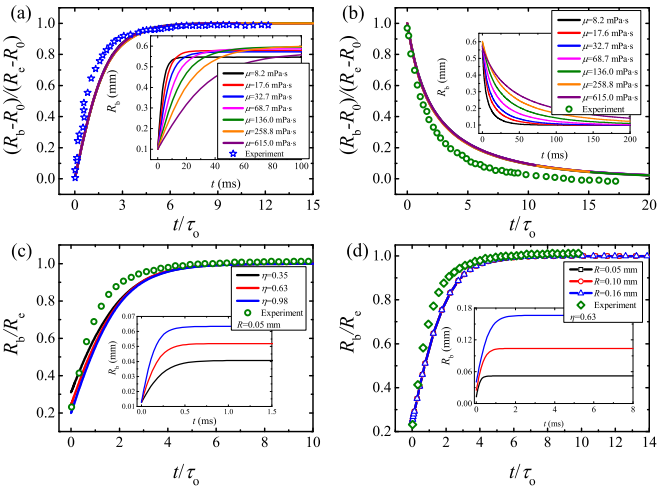

FIG. 3. Plots of rescaled base radius $(R_b - R_0)/(R_e - R_0)$ vs normalized time t/τ_o for (a) spreading stage and (b) recoiling stage, with parameter values $U = 80$ V and $R = 1$ mm. Plots of normalized spreading base radius R_b/R_e vs normalized time t/τ_o for different (c) EW numbers η and (d) droplet sizes R. The experimental data in (a) and (b), and (c) and (d) come from Ref. [19] and Ref. [18], respectively.

droplet viscosities during the EW and retraction processes in Figs. 3(a) and 3(b), where the insets are the corresponding raw results of each plot. Here the time of evolution is rescaled as t/τ_o, while the base radius is done as $(R_b - R_0)/(R_e - R_0)$. Notably, the rescaled base radius follows a master curve, demonstrating that the normalized time-dependent base radius is independent of liquid viscosities. In contrast, the insets in Figs. 3(a) and 3(b) illustrate the effects of liquid properties.

Figures 3(c) and 3(d) show the effects of applied voltage and droplet size on spreading base radius. The base radius is normalized by the base radius at the final equilibrium state, and insets demonstrate plots of R_b versus t prior to normalization. Similarly, the normalized evolutions collapse to a master curve independent of applied voltage and droplet size, indicating that timescale τ_o can be used to characterize the transient dynamics in the overdamped regime. This can be ascribed to the fact that the viscous dissipation in the bulk has been neglected. In addition, experimental data from Refs. [18] and [19] are also shown in Fig. 3, where the good agreement between our model and experiments verifies that the present theoretical model based on the Onsager variational principle is suitable to interpret the nonequilibrium EW-driven droplet dynamics.

B. Underdamped regime

Besides the overdamped regime, we also investigate the spreading dynamics of droplets with low viscosity, namely, the underdamped regime. Our calculation is performed by using the values of parameters $\varepsilon = 1.93$, $d = 2.5$ mm, $\mu_0 = 4.6$ mPa s, and $C = 32.9$ [18]. All the summations in the paper were carried out over $n = 120$. In the underdamped regime, our analysis of EW dynamics is based on the derived shape equation Eq. (21); thus it is necessary to verify the validity of the present model. For this reason we examine whether the

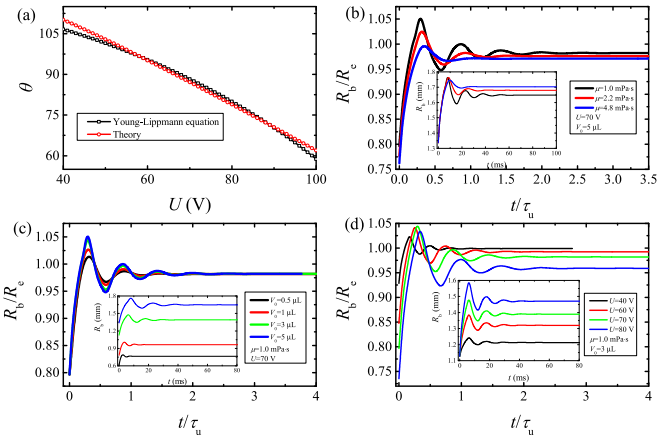

FIG. 4. (a) Comparison of contact angle predicted by the present model with that calculated by the Young-Lippmann equation. Plots of normalized spreading base radius R_b/R_e vs normalized time t/τ_u for different (b) droplet viscosities μ, (c) applied voltages U, and (d) droplet volumes V_0.

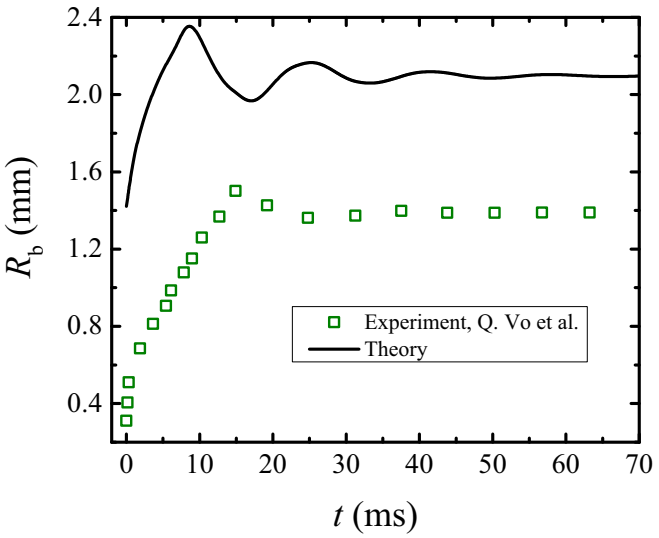

FIG. 5. Comparison of theoretical time-dependent base radius R_b with the experimental data measured by Vo *et al.* in Ref. [18] for the underdamped regime.

apparent contact angle at equilibrium state predicted by our model is consistent with the well-known Young-Lippmann equation [1,31] $\cos\theta_L = \cos\theta_Y + \varepsilon_0\varepsilon U^2/(2d\gamma_{lm})$. We numerically calculate the apparent contact angle by utilizing Eq. (27) in Ref. [28], and the comparison between the contact angle predicted by the present model and those of Young-Lippmann equation is demonstrated in Fig. 4(a). It is observable that the calculated contact angle based on the present model agrees very well with that of the Young-Lippmann equation, an evidence once again confirming the validity of the present model.

Subsequently, in order to reveal how droplet viscosity, droplet size, and applied voltage affect the spreading dynamics driven by EW, we plot the normalized spreading base radius R_b/R_e versus normalized time t/τ_u for various controlling factors (liquid viscosity, droplet size, and applied voltage), as demonstrated in Figs. 4(b), 4(c) and 4(d). The insets show the corresponding un-normalized R_b. In the figure it is found that a smaller droplet with higher viscosity under lower voltage activation reaches its maximum peak and equilibrium shape faster than a larger droplet with lower viscosity. Here τ_u is the characteristic timescale for the droplet to reach maximum deformation in the underdamped regime, which is given by $\tau_u = \pi\rho^{1/2}R^{3/2}/(\eta\gamma_{lm})^{1/2}$ based on the balance between the driving force and droplet's inertia with the viscosity neglected [18,34]. The time evolution of the normalized spreading base radius in Fig. 4 indicates that R_b monotonically increases to the first peak and reaches the maximum deformation in the beginning, followed by a damped oscillation, and eventually approaches a stable equilibrium state. The apparent oscillation at the droplet's surface stems from the from the fact that the droplet's inertia resists the contact line motion, even though eventually the corresponding energy is absorbed by the contact line as a result of dissipation. The conclusion that τ_u is a characteristic timescale in the underdamped regime does not change for different controlling parameters such as droplet viscosity [Fig. 4(b)], droplet size [Fig. 4(c)], and applied voltage [Fig. 4(d)]. Our theoretical predictions also agree well with the experimental results reported in Refs. [18,24,28].

In order to examine the oscillating profiles in Figs. 4(b), 4(c), and 4(d), we further make a comparison with the experimental results observed by Vo *et al.* in Ref. [18], as shown in Fig. 5. Basically, our model shows the typical oscillating features detected by experiments in the underdamped regime. Nevertheless, the theoretical equilibrium base radius is found to be larger than that measured by experiment. The reason lies in the different initial contact angle between theoretical calculations (90°) and experiment (about 164°) under the same droplet volume results.

Consequently, the good agreement between theoretical prediction and experimental results suggests that both the spreading and the retraction dynamics driven by EW can be captured by our proposed theoretical model. In the overdamped regime, the damping effect due to viscous dissipation and friction dominates the whole spreading or the retraction process, which makes the droplet to spread or retract gradually to its equilibrium configuration without oscillation while keeping its spherical shape profile. In this regime, the transient dynamics can be characterized by a typical timescale τ_o, whereas in the underdamped regime the inertial effect is comparable with the damping effect, resulting in an apparent oscillation on the droplet's surface. Similarly, its transient dynamics can be characterized by a timescale τ_u. It is found that the characteristic timescales τ_o and τ_u are independent of liquid viscosity, droplet size, and applied voltage.

IV. CONCLUSION

In summary, we develop a theoretical model to explicitly formulate the nonequilibrium free energy in terms of shape parameters for a viscous droplet immersed in an ambient environment by using the Onsager principle and obtain a set of shape equations governing the EW-driven droplet dynamics. The excellent agreement between our numerical results and

the corresponding experimental ones shows that our model captures the essential phenomena of the dynamic behaviors of both spreading and retraction driven by EW. Our theoretical results also reveal that the transient dynamics of viscous droplets can be characterized by a typical timescale τ_o or τ_u for the overdamped or the underdamped regime, respectively. Such characteristic timescales are independent of liquid viscosity, droplet size, and applied voltage.

ACKNOWLEDGMENTS

We acknowledge financial support from the National Natural Science Foundation of China under Grants No. 12147142, No. 11974292, and No. 12174323, and 111 Project No. B16029. Thanks are also given to Xi Chen, Wei Li, Dr. Rui Ma, and Dr. Xuezheng Cao for helpful discussions.

APPENDIX: THE DERIVATION OF EQUATIONS (6), (14), and (17)

For the overdamped regime, during the spreading and recoiling processes, the droplet volume can be calculated as

$$V^{o}(t) = \frac{\pi R_b^3 (2 - 3\cos\theta + \cos^3\theta)}{3\sin^3\theta}. \tag{A1}$$

Due to the conservation of droplet volume $dV^o/dt = (\partial V^o/\partial R_b)\dot{R}_b + (\partial V^o/\partial\theta)\dot{\theta} = 0$, we have

$$\pi R_b^2 \frac{(2+\cos\theta)(1-\cos\theta)^2}{\sin^3\theta}\dot{R}_b + \frac{\pi R_b^3 (1-\cos\theta)^2}{\sin^4\theta}\dot{\theta} = 0. \tag{A2}$$

By simplifying the above equation, then we can get Eq. (6) in the main text.

For the underdamped regime, the change of the volume ΔV due to the deformation of the droplet is given by [46]

$$\Delta V = 2\pi R_0^2 c_0(t) + 2\pi R_0 \sum_{n=1}^{\infty} \frac{c_{2n}^2(t)}{4n+1}. \tag{A3}$$

Thus the total volume of the droplet can be calculated as

$$V^{u} = V_0 + \Delta V, \tag{A4}$$

where $V_0 = 2\pi R_0^3/3$ is the volume of the droplet before deformation. The conservation of droplet volume $dV^u/dt = 0$ yields Eq. (17). Let the deformation of the hemispherical droplet shape be expressed as

$$\delta R = \sum_{n=1}^{\infty} c_{2n}(t) P_{2n}(\cos\varphi), \tag{A5}$$

and the surface of the droplet to the origin of the droplet is $r = R_0 + \delta R$. Then the area of the liquid-medium interface can be calculated as [46]

$$A_{lm} = 2\pi R_0^2 + 4\pi R_0 c_0(t) + 2\pi \sum_{n=1}^{\infty} \frac{n(2n+1)+1}{4n+1} c_{2n}^2(t). \tag{A6}$$

The area of the liquid-solid interface is given by (to the first order of δR)

$$A_{ls} = \pi R_0^2 + 2\pi R_0 \sum_{n=1}^{\infty} c_{2n}(t) P_{2n}(0). \tag{A7}$$

Substituting Eqs. (A6) and (A7) into Eq. (2) in the main text yields Eq. (14).

[1] F. Mugele and J. C. Baret, Electrowetting: From basics to applications, J. Phys.: Condens. Matter **17**, R705 (2005).
[2] K. Choi, A. H. C. Ng, R. Fobel, and A. R. Wheeler, Digital microfluidics, Annu. Rev. Anal. Chem. **5**, 413 (2012).
[3] S. Jun Lee, S. Lee, and K. Hyoung Kang, Droplet jumping by electrowetting and its application to the three-dimensional digital microfluidics, Appl. Phys. Lett. **100**, 081604 (2012).
[4] P. G. Zhu and L. Q. Wang, Passive and active droplet generation with microfluidics: A review, Lab Chip **17**, 34 (2017).
[5] J. Hong and S. J. Lee, Detaching droplets in immiscible fluids from a solid substrate with the help of electrowetting, Lab Chip **15**, 900 (2015).
[6] R. A. Hayes and B. J. Feenstra, Video-speed electronic paper based on electrowetting, Nature (London) **425**, 383 (2003).
[7] C. L. Hao, Y. H. Liu, X. M. Chen, Y. C. He, Q. S. Li, K. Y. Li, and Z. K. Wang, Electrowetting on liquid-infused film (EWOLF): Complete reversibility and controlled droplet oscillation suppression for fast optical imaging, Sci. Rep. **4**, 6846 (2014).
[8] S. Kuiper and B. H. W. Hendriks, Variable-focus liquid lens for miniature cameras, Appl. Phys. Lett. **85**, 1128 (2004).
[9] J. Heikenfeld and A. J. Steckl, High-transmission electrowetting light valves, Appl. Phys. Lett. **86**, 151121 (2005).
[10] T. Boland, T. Xu, B. Damon, and X. F. Cui, Application of inkjet printing to tissue engineering, Biotechnol. J. **1**, 910 (2006).
[11] L. B. Zhang, J. B. Wu, M. N. Hedhili, X. L. Yang, and P. Wang, Inkjet printing for direct micropatterning of a superhydrophobic surface: Toward biomimetic fog harvesting surfaces, J. Mater. Chem. A **3**, 2844 (2015).
[12] K. M. Wisdom, J. A. Watson, X. Qu, F. Liu, G. S. Watson, and C. H. Chen, Self-cleaning of superhydrophobic surfaces by self-propelled jumping condensate, Proc. Natl. Acad. Sci. USA **20**, 7992 (2013).
[13] Q. L. Zhang, M. He, J. Chen, J. J. Wang, Y. L. Song, and L Jiang, Anti-icing surfaces based on enhanced self-propelled jumping of condensed water microdroplets, Chem. Commun. **49**, 4516 (2013).
[14] J. B. Boreyko and C. H. Chen, Self-Propelled Dropwise Condensate on Superhydrophobic Surfaces, Phys. Rev. Lett. **103**, 184501 (2009).
[15] K. Xiao and C. X. Wu, Curvature effect of electrowetting-induced droplet detachment, J. Appl. Phys. **129**, 234701 (2021).
[16] K. Xiao, X. Chen, and C. X. Wu, Electric field-triggered Cassie-Baxter-Wenzel wetting transition on textured surface, Phys. Rev. Research **3**, 033277 (2021).

[17] F. Mugele, Fundamental challenges in electrowetting: From equilibrium shapes to contact angle saturation and drop dynamics, Soft Matter **5**, 3377 (2009).
[18] Q. Vo, H. B. Su, and T. Tran, Universal transient dynamics of electrowetting droplets, Sci. Rep. **8**, 836 (2018).
[19] Q. Vo and T. Tran, Contact line friction of electrowetting actuated viscous droplets, Phys. Rev. E **97**, 063101 (2018).
[20] T. D. Blake and J. M. Haynes, Kinetics of liquid/liquid displacement, J. Colloid Interface Sci. **30**, 421 (1969).
[21] L. H. Tanner, The spreading of silicone oil drops on horizontal surfaces, J. Phys. D: Appl. Phys. **12**, 1473 (1979).
[22] P. K. Mondal, D. DasGupta, A. Bandopadhyay, U. Ghosh, and S. Chakraborty, Contact line dynamics of electroosmotic flows of incompressible binary fluid system with density and viscosity contrasts, Phys. Fluids **27**, 032109 (2015).
[23] J. C. Bird, S. Mandre, and H. A. Stone, Short-Time Dynamics of Partial Wetting, Phys. Rev. Lett. **100**, 234501 (2008).
[24] J. Hong, Y. K. Kim, K. H. Kang, J. M. Oh, and I. S. Kang, Effects of drop size and viscosity on spreading dynamics in DC electrowetting, Langmuir **29**, 9118 (2013).
[25] M. Marinescu, M. Urbakh, T. Barnea, A. R. Kucernak, and A. A. Kornyshev, Electrowetting dynamics facilitated by pulsing, J. Phys. Chem. C **114**, 22558 (2010).
[26] H. Li, M. Paneru, R. Sedev, and J. Ralston, Dynamic electrowetting and dewetting of ionic liquids at a hydrophobic solid-liquid interface, Langmuir **29**, 2631 (2013).
[27] J. M. Oh, S. H. Ko, and K. H. Kang, Shape oscillation of a drop in ac electrowetting, Langmuir **24**, 8379 (2008).
[28] J. M. Oh, S. H. Ko, and K. H. Kang, Analysis of electrowetting-driven spreading of a drop in air, Phys. Fluids **22**, 032002 (2010).
[29] S. R. Annapragada, S. Dash, S. V. Garimella, and J. Y. Murthy, Dynamics of droplet motion under electrowetting actuation, Langmuir **27**, 8198 (2011).
[30] Q. Zhao and W. Ren, A finite element method for electrowetting on dielectric, J. Comput. Phys. **429**, 109998 (2021).
[31] G. Lippmann, Relation entre les phénomènes électriques et capillaires, Ann. Chim. Phys. **5**, 494 (1875).
[32] A. Cavalli, D. J. Preston, E. Tio, D. W. Martin, N. Miljkovic, E. N. Wang, F. Blanchette, and J. W. M. Bush, Electrically induced drop detachment and ejection, Phys. Fluids **28**, 022101 (2016).
[33] K. X. Zhang, Z. Li, and S. Chen, Analytical prediction of electrowetting-induced jumping motion for droplets on hydrophobic substrates, Phys. Fluids **31**, 081703 (2019).
[34] Q. Vo and T. Tran, Critical Conditions for Jumping Droplets, Phys. Rev. Lett. **123**, 024502 (2019).
[35] M. Doi, Onsager's variational principle in soft matter, J. Phys.: Condens. Matter **23**, 284118 (2011).
[36] M. Doi, *Soft Matter Physics* (Oxford University Press, New York, 2013).
[37] M. Doi, Onsager principle as a tool for approximation, Chin. Phys. B **24**, 020505 (2015).
[38] O. V. Voinov, Hydrodynamics of wetting, Fluid Dyn. **11**, 714 (1976).
[39] R. G. J. Cox, The dynamics of the spreading of liquids on a solid surface, Part 1. Viscous flow, J. Fluid Mech. **168**, 169 (1986).
[40] F. Brochard-Wyart and P. G. de Gennes, Dynamics of partial wetting, Adv. Colloid Interface Sci. **39**, 1 (1992).
[41] X. Xu, Y. Di, and M. Doi, Variational method for liquids moving on a substrate, Phys. Fluids **28**, 087101 (2016).
[42] A. Carlson, G. Bellani, and G. Amberg, Contact line dissipation in short-time dynamic wetting, Europhys. Lett. **97**, 44004 (2012).
[43] K. H. Kang, How electrostatic fields change contact angle in electrowetting, Langmuir **18**, 10318 (2002).
[44] Q. G. Wang, M. Xu, C. Wang, J. P. Gu, N. Hu, J. F. Lyu, and W. Yao, Actuation of a nonconductive droplet in an aqueous fluid by reversed electrowetting effect, Langmuir **36**, 8152 (2020).
[45] W. Ren and W. E, Boundary conditions for the moving contact line problem, Phys. Fluids **19**, 022101 (2007).
[46] Z. Zhang, Y. Wang, Y. Amarouchene, R. Boisgard, H. Kellay, A. Würger, and A. Maali, Near-Field Probe of Thermal Fluctuations of a Hemispherical Bubble Surface, Phys. Rev. Lett. **126**, 174503 (2021).
[47] Z. Q. Sun, L. Zhuang, M. Y. Wei, H. L. Sun, F. L. Liu, B. Tang, J. Groenewold, and G. F. Zhou, Bubble manipulation driven by alternating current electrowetting: Oscillation modes and surface detachment, Langmuir **37**, 6898 (2021).